ELSEVIER

Physica C 269 (1996) 255–267

PHYSICA C

Bi-epitaxial YBCO grain boundary Josephson junctions on $SrTiO_3$ and sapphire substrates

S. Nicoletti [a,*], H. Moriceau [b], J.C. Villegier [a], D. Chateigner [c], B. Bourgeaux [c], C. Cabanel [d], J.Y. Laval [d]

[a] *DRFMC / SPSMS – CEA Grenoble, 38054 Grenoble Cedex 09 France*
[b] *LETI / DMITEC, 38054 Grenoble Cedex 09 France*
[c] *CNRS-Laboratoire de Cristallographie, BP 166, 38042 Grenoble Cedex 09 France*
[d] *Laboratoire de Physique du Solide UPR 5 CNRS-ESPCI, 10, rue Vauquelin, 75231 Paris Cedex 05 France*

Received 26 February 1996; revised manuscript received 24 June 1996

Abstract

This paper deals with YBCO Josephson junctions based on artificially generated in-plane bi-epitaxial grain boundaries fabricated on $SrTiO_3$ and buffered R-plane sapphire. The grain boundary was obtained by partly interposing a MgO seed layer between a bare or even-buffered substrate and a CeO_2 layer [1]. The devices were produced by patterning the overhanging YBCO film in a form of stripes across the grain boundary occurring at the interface between the two regions.

The samples were structurally and electrically characterized. As shown by X-ray diffraction analyses and high resolution electron microscopy, the structural perfection of the YBCO film decreases as the complexity of the stacking sequence increases. The fabricated junctions behave according to the Resistively Shunted Junction model for both the samples on $SrTiO_3$ and on Al_2O_3. Under microwave irradiation, the devices displayed several Shapiro steps while their critical currents were deeply modulated under magnetic field.

By comparing the transport properties of the devices with the structural properties of the YBCO film on the different stacking sequences, we found a strong correlation between the normalized resistance $R_N A$ and the degree of structural disorder in the superconducting film.

Keywords: Grain boundary; Texturing; Thin films; Weak links; Josephson effect

1. Introduction

Large angle grain boundaries (GB) are well known to behave like a weak link with RSJ behavior [2]. The fabrication of complex devices based on GB junctions actually represents one of the most viable ways to develop superconducting electronic circuits. In this aim the control of artificial GBs in the YBCO films is essential.

GB junctions obtained on bi-crystal substrates show good junction quality and reproducibility and among the best performances [3] but the intrinsic restrain of the GB location at the bi-crystal interface seriously limit their integration in any large scale technological process. Moreover, this technique is

* Corresponding author. Permanent address: CNR-Istituto LAMEL, Via Gobetti 101, I-40129 Bologna, Italy. Fax: +39 51 6399216; e-mail: nicoletti@area.bo.cnr-it.

PII S0921-4534(96)00468-6

well assessed for $SrTiO_3$ (STO) or MgO [4] but for other substrates of technological interest, such as Al_2O_3 (ALO), several problems are still present.

A possible way to overcome these problems is the fabrication of artificially engineered bi-epitaxial GB [1,5,6], where a suitable sequence of epitaxial layers locally induce a 45° rotation of the crystal lattices across the grain boundary. This behavior, first shown at Conductus [1], has to be related to an "abnormal" epitaxial in plane coincidence between the MgO and the CeO_2 crystal lattices where MgO is a very thin "seed" film independent of the underlying substrate. It is worth noting that the use of commercially available, low cost epitaxial quality R-plane sapphire substrates, should be envisaged for any application where high dielectric constant and low losses are required. However, for this kind of substrates, severe film-substrate interactions occurring above 650°C require a buffer layer as a barrier against the diffusion.

In this paper we report the fabrication and the characterization of bi-epitaxial 45° GB Josephson junctions on $SrTiO_3$ (STO) or Al_2O_3 (ALO) substrates. This work is focused on the MgO–CeO_2 seed layers deposition and on the CeO_2/YBCO/STO multilayer buffer for the sapphire substrates suitable for a collective fabrication of artificially engineered GB with good reproducibility of the process. Emphasis is made on the structural properties of the stacking sequence and on their influence on the electrical performances of the final device.

2. Experimental

The films depositions were carried out by Pulsed Laser Deposition (PLD) from sintered massive targets. The PLD apparatus used is based on an excimer laser ($\lambda = 248$ nm, $\tau_{pulse} = 30$ ns). The deposition chamber is equipped with four targets and with a load lock, allowing multilayer processes without breaking vacuum or atmosphere. All the deposition parameters are controlled by a personal computer insuring good reproducibility. A detailed description of the deposition apparatus was reported elsewhere [7].

It is well known that in the temperature range of the YBCO deposition, STO is chemically stable while sapphire presents a severe interdiffusion between the substrate and the superconducting film. To obtain both a suitable crystal lattice and a barrier against the mutual diffusion a CeO_2/YBCO/STO trilayer was first deposited on the sapphire substrates. This multilayer structure was chosen to overcome the limitations in the stacking sequence. The STO thin films do not grow epitaxialy nor on R-plane ALO neither on CeO_2 films, giving several orientations and a large fraction of amorphous material. The deposition of the CeO_2/YBCO/STO tri-layer allows an epitaxial growth along the whole structure of the buffer layer as well as a suitable substrate surface for the fabrication of the bi-epitaxial GB.

In order to fabricate artificially engineered bi-epitaxial grain boundaries, a ~ 5 nm thick MgO seed layer and a ~ 11 nm thick CeO_2 buffer layer were first deposited onto a bare (or buffered) substrate under the same processing conditions. These two intermediate layers were therefore removed on part of the substrate by Xe ion milling on a photolithographically defined geometry. These procedures lead to a smooth and sharp interface where the grain boundary is located. Then a second ~ 18 nm CeO_2 buffer layer and the superconducting YBCO film were deposited. The PLD process parameters for each deposition step are summarized in Table 1 while Fig. 1(a,b) shows the stacking sequence followed during the fabrication process for STO and ALO, respectively. To define the contact pads, a 200 nm thick gold layer was subsequently sputtered through a mechanical mask. The devices were patterned in form of stripes defined across the GB by standard photolithographic technique followed by Xe ion milling.

The films obtained were structurally characterized by X-ray diffraction analysis (XRD) in both the Bragg–Brentano and Schulz [8] configurations using the Cu-Kα radiation and by Transmission Electron Microscopy (TEM). Using XRD, we measured the θ–2θ scans, and pole figures on the part of the sample where the MgO is present and on the part of the sample where the MgO was removed. By means of these analyses we first determined the in-plane epitaxial relationships and then, considering the pole dispersion taken at their full width half maximum (FWHM), we evaluated the degree of orientation. The experimental setup and the axes resolutions were described elsewhere [9] as well as the calcula-

tion procedure to obtain the volume fraction related to a given peak [10].

The samples on STO were observed on cross-sections, by high resolution electron microscopy (HTEM). In order to prepare these specimens, two flakes heterostructures were glued together with an epoxy charged with a very fine alumina powder (0.5 μm). The obtained disks were cut with their faces perpendicular to the [100] axis of the substrate. Then they were mechanically thinned to $\cong 15$ μm and ion milled at low temperature to electron transparency. Cross-sections were observed at 200 keV on a Philips CM20UT.

The electrical characterization was performed by placing the samples on a cryogenic probe for testing under magnetic field as well as under microwave irradiation. The probe was inserted in a double magnetic shielded dewar allowing the measurements from

Table 1
Deposition parameters used during the fabrication of bi-epitaxial grain boundaries

Material	Sub-layer or substrate	Temperature (°C)	Laser energy (J/cm^2)	Pulse rate (Hz)	Oxygen pressure (Pa)	Deposition rate (nm/pulse)	Thickness (nm)
CeO_2	R-Al_2O_3	780	2.0	1	40	0.05	20
YBCO	CeO_2	650	2.0	2	40	0.06	30
$SrTiO_3$	YBCO	780	2.6	5	32	0.02	50
MgO	$SrTiO_3$	600	2.6	5	2.5	0.009	5
CeO_2-I	MgO	780	2.0	10	40	0.05	11
CeO_2-II	CeO_2-I/$SrTiO_3$	780	2.0	10	40	0.05	18
YBCO	CeO_2	750–780	2.0	2	40	0.055	200

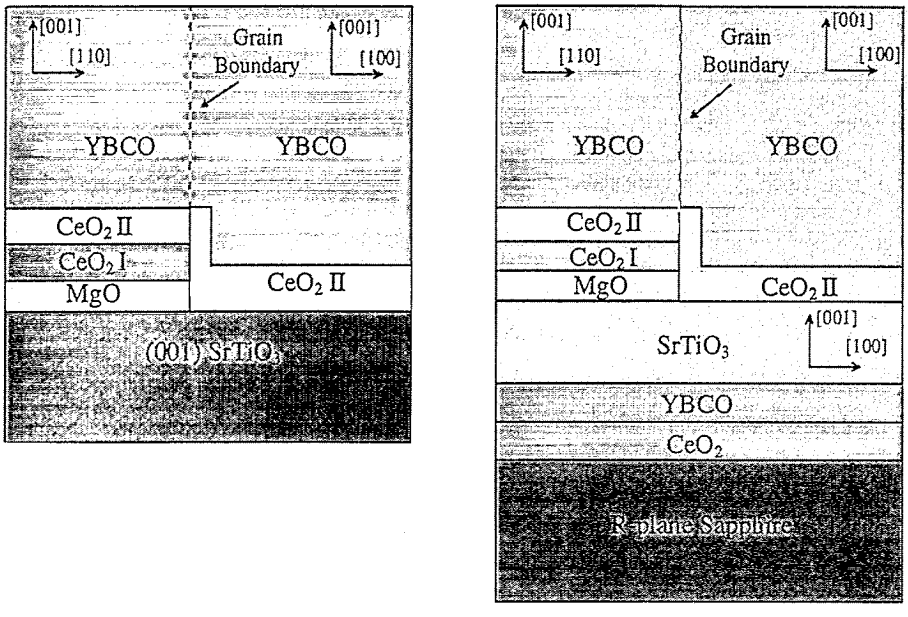

Fig. 1. Schematic representation of the stacking sequence followed during the grain boundary fabrication on a) $SrTiO_3$ and b) R-plane sapphire substrates, respectively.

room temperature to liquid helium temperature. The data were collected by taking as a general criterion for the J_c evaluation the current value corresponding to a 10 μV voltage drop across the junction.

3. Results and discussion

3.1. Structural characterization

The XRD θ–2θ scans allow the determination of the crystalline planes parallel to the sample surface. In Figs. 2 and 3 we report the θ–2θ diffraction patterns of two different samples deposited on STO and ALO substrates, respectively. To facilitate the comparison, the patterns collected on the whole stacking sequence were shifted with regard to those collected on the side where the MgO/CeO_2 bi-layer was etched. Two general features can be observed. First, as indicated by the strong (00l) reflections, the YBCO and the MgO layers are mainly grown [001] oriented. The presence of the characteristic $BaCeO_3$ (BCO) reflections indicates that some reactions occur at the interface between YBCO and CeO_2 layers.

The CeO_2 layers behave differently, depending on the substrate side. As shown by the diffraction patterns of Fig. 2, on STO substrate we can identify two different behaviors: on bare substrate, the CeO_2 is (001)-oriented even after the ion etching. Where MgO is present underneath the CeO_2 layer, we observe a strong reflection at $2\theta \cong 29.5$. This additional peak can be attributed either to (111) reflection of CeO_2 or to the (200 + 112) reflections from the BCO. Furthermore, the growth of this phase seems to be competing with the growth of the BCO phase, as evidenced by the (004 + 220) reflection of this latter phase which decreases considerably in intensity when (111)-CeO_2 increases (4 layers side). This is consistent with less $YBCO/CeO_2$ interaction when the etching procedure has been applied (less crystalline disorder in the CeO_2 layer in the absence of MgO). The poor crystallinity of CeO_2 and BCO, whatever the substrate and the sample side, is revealed by comparing the enlargement of their peaks with those of the YBCO in the θ–2θ spectra. The (111)-CeO_2 and (200 + 112)-BCO reflections are too

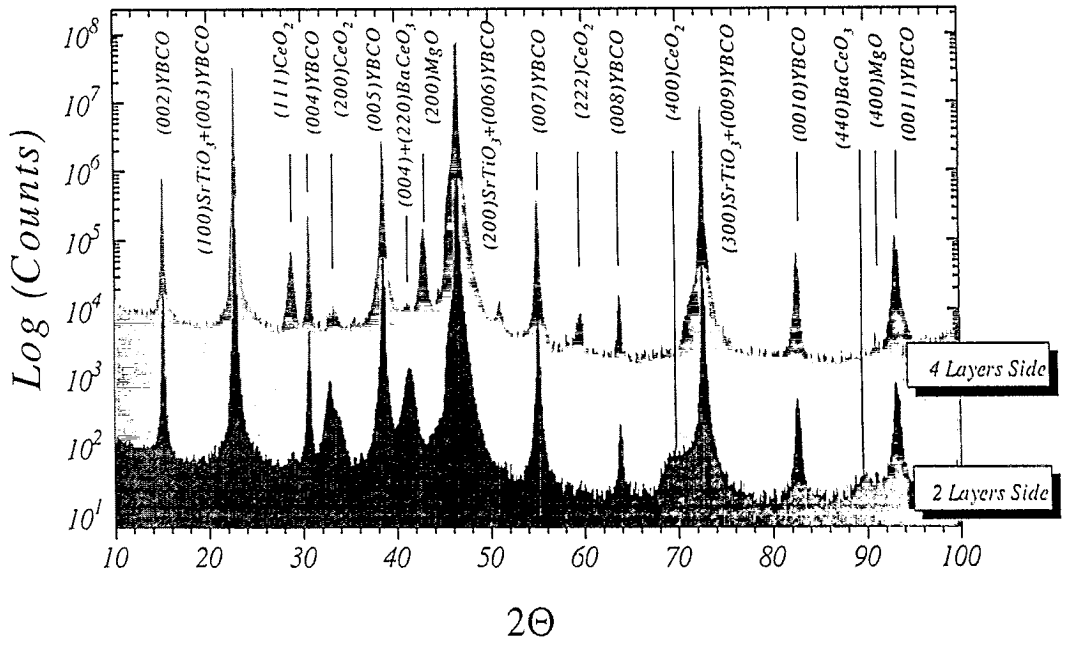

Fig. 2. θ–2θ diffraction patterns collected on both halves of a sample fabricated on $SrTiO_3$ substrate. The pattern collected on the whole stacking sequence is [4 layers side] shifted with regards to that collected on the side without the MgO/CeO_2 bi-layer [2 layers side].

close (28.5–29.5 in θ) to be distinguished taking into account the peak width.

As reported in Fig. 3, the same set of peaks was found on sapphire substrate, with the exception of those coming from the substrate itself. Taking into account that a buried double layer of CeO_2/YBCO is first deposited on this substrate, we attribute the (004 + 220)-BCO peak (present on both sides) to this first deposited layer. Since this deep layer partially shadows the duality between the (111)-CeO_2 and the (004 + 220)-BCO peaks, we can assume a similar behavior for this stacking sequence.

Fig. 4 shows HREM cross-section images corresponding to the grown heterostructures a) without the MgO layer and b) with the MgO layer, respectively. From Fig. 4a we found, for both the CeO_2 and YBCO grown on STO, the same orientation relationships already detected by X-ray analyses. The YBCO layer grows with the same orientation as the substrate. The STO/CeO_2 interface is fairly abrupt whereas the CeO_2/YBCO interface is highly perturbed as a result a preferential thinning on the YBCO side; the thickness of the CeO_2 layer is found to be equal to 11 nm. The BCO phase, observed by X-ray, was not detected in this region. This behavior can be explained by assuming that the BCO is present only as islands.

From the micrograph 4b we found that the YBCO layer is 45° rotated along the c axis, whenever a MgO layer is intercalated in the growth process. The MgO and CeO_2 layers are 4 nm and 30 nm thick, respectively. The interfaces are well defined and sharp. However, in the CeO_2 layer we can distinguish two different zones. Close to the MgO interface, the presence of Moiré patterns reveals slight local variations of the lattice parameters and a fairly perturbed layer. Nevertheless the lattice parameter length indicates an (00l)-oriented growth. Otherwise, close to the YBCO interface, the lattice parameter changes, indicating the formation of a different phase. This phase can be identified as either (111)-oriented CeO_2 or (200)-oriented BCO. Since the thickness almost coincides with that expected for the topmost CeO_2 layer and the (111)-phase admits the growth of

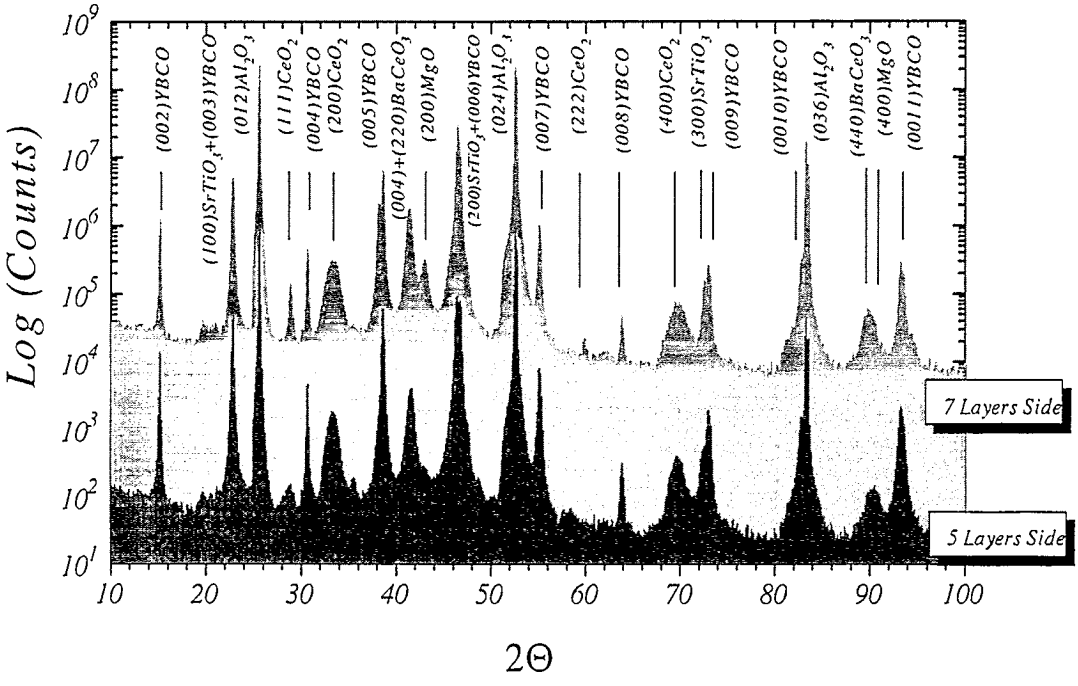

Fig. 3. θ–2θ diffraction patterns collected on both halves of a sample fabricated on Al_2O_3 substrate. The pattern collected on the whole stacking sequence [7 layers side] is shifted with regards to that collected on the side without the MgO/CeO_2 bi-layer [5 layers side].

the (00l)-YBCO layer along the suitable in-plane orientation, we attribute the peak located at $2\theta \cong 29.5$ to this phase.

In Fig. 5 we report a ϕ-scan of a STO sample while Fig. 6 displays the pole figure of an ALO sample. Each sample were scanned on both sides. In

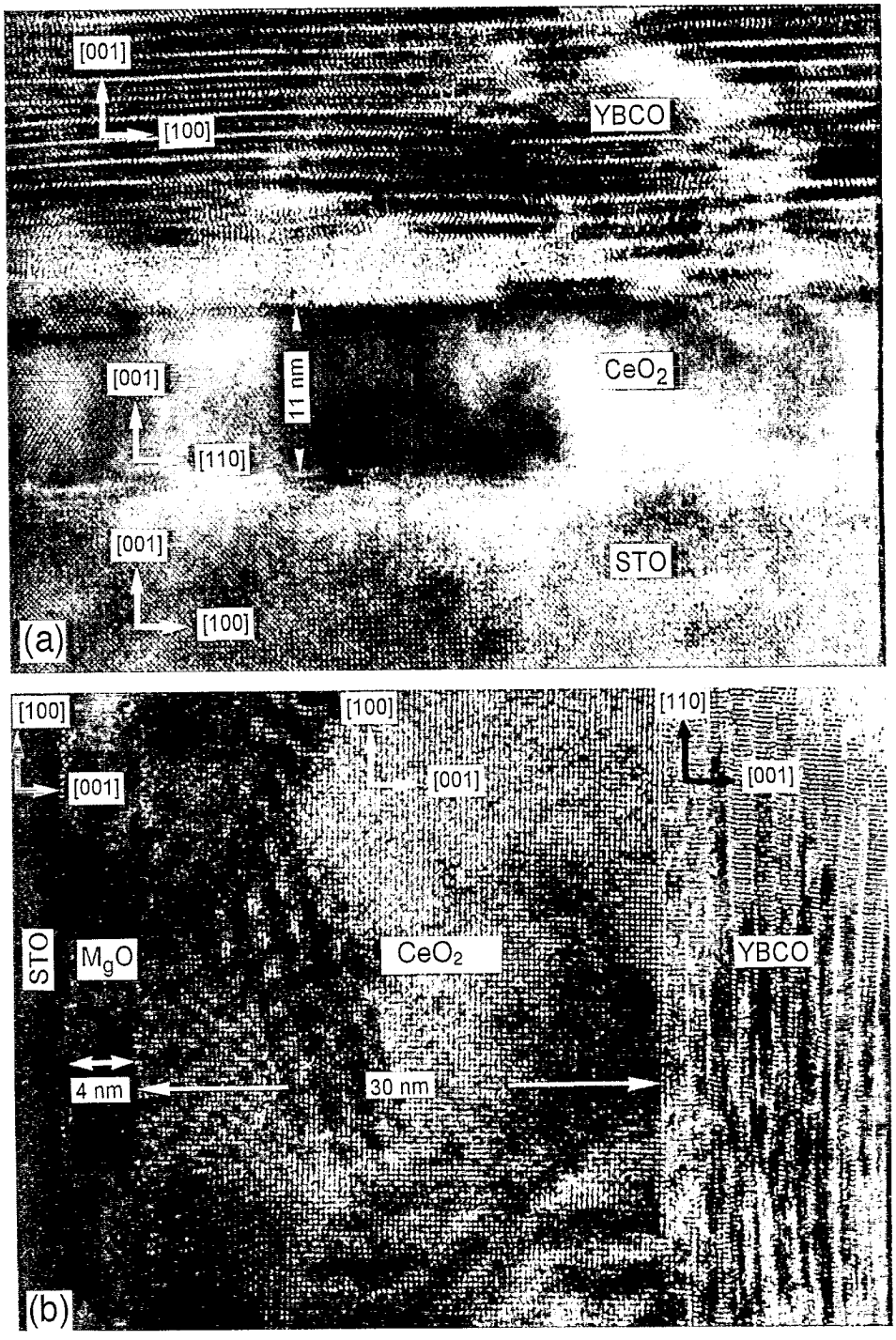

Fig. 4. HREM cross view of a) the YBCO/CeO_2 and b) the YBCO/CeO_2/MgO multilayers structure on a $SrTiO_3$ substrate.

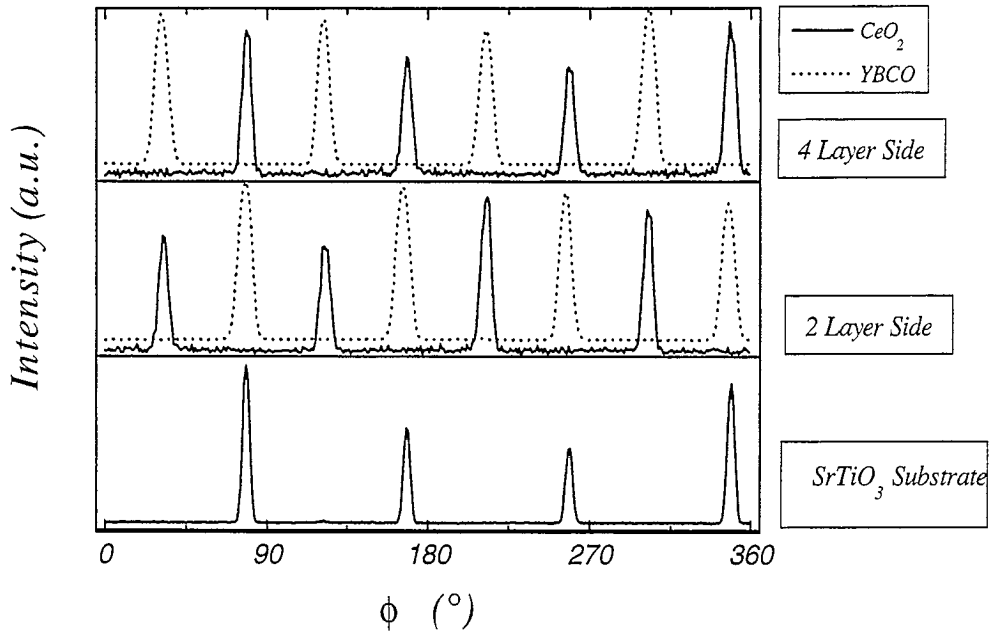

Fig. 5. ϕ-scan diffraction pattern of the {204}-CeO2 and {108}-YBCO reflections taken separately on both sides of an $SrTiO_3$ sample. The diffraction pattern of {204} of the substrate is reported for comparison, in the bottom of the figure.

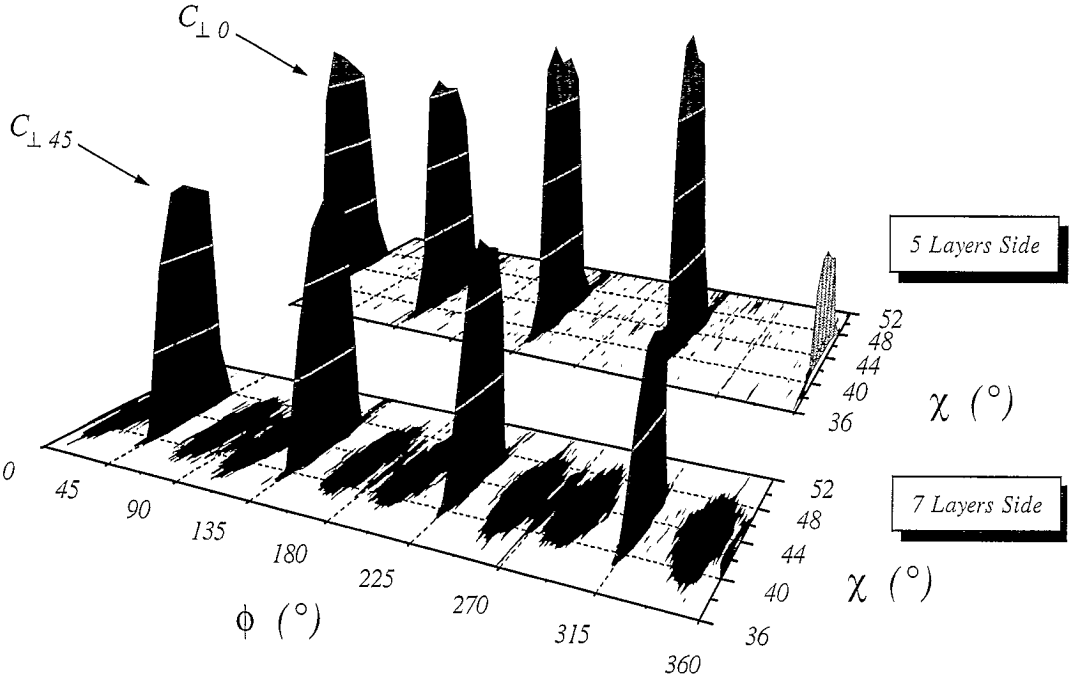

Fig. 6. Pole figure diffraction pattern of the {103}-YBCO reflection taken separately on both sides of a sample fabricated on sapphire substrate.

Table 2
Epitaxial relationships between substrates and deposited layers

Substrate material	Relationship	Sample area without the MgO seed layer	Sample area with the MgO seed layer
$SrTiO_3$	Perpendicular to the substrate surface	[001]YBCO‖[001]CeO_2‖[001]$SrTiO_3$	[001]YBCO‖[001]CeO_2‖[001]MgO‖[001]$SrTiO_3$
	Parallel to the substrate	[100]YBCO‖[110]CeO_2‖[100]$SrTiO_3$	[110]YBCO‖[100]CeO_2‖[100]MgO‖[100]$SrTiO_3$
Al_2O_3	Perpendicular to the substrate surface	[001]YBCO‖[001]CeO_2‖[001]$SrTiO_3$‖[001]YBCO‖[001]CeO_2‖[012]*Al_2O_3	[001]YBCO‖[001]CeO_2‖[001]MgO[001]$SrTiO_3$‖[001]YBCO‖[001]CeO_2‖[012]*Al_2O_3
	Parallel to the substrate surface	[100]YBCO‖[110]CeO_2‖[100]$SrTiO_3$‖[100]YBCO‖[110]CeO_2‖[021]Al_2O_3	[110]YBCO‖[100]CeO_2‖[100]MgO[100]$SrTiO_3$‖[100]YBCO‖[110]CeO_2‖[021]Al_2O_3

the case of STO (Fig. 5), as expected from the cell match between the different layers, the relationships are fully respected for both sides of the GB. The $C_{\perp 0}^{YBCO}$ relationship is the only one present when the MgO is absent (2 layers), while when it is present (4 layers) $C_{\perp 45}^{YBCO}$ is fully achieved. In the case of ALO (Fig. 6), $C_{\perp 0}^{YBCO/STO}$ is also fully respected when MgO is absent (5 layers), but persists at a level of 1–2% in volume on the 7 layers side of the sample. The buried YBCO layer deposited together with CeO_2 and STO to buffer the ALO can account for this residual orientation. The $C_{\perp 45}^{YBCO}$ attempted relationship dominates with ~94% in volume on this side of the GB, even if we can observe the presence of $C_{\perp \phi}^{YBCO}$ orientations with $8° \leq \phi \leq 30°$ of about 3–4% in volume.

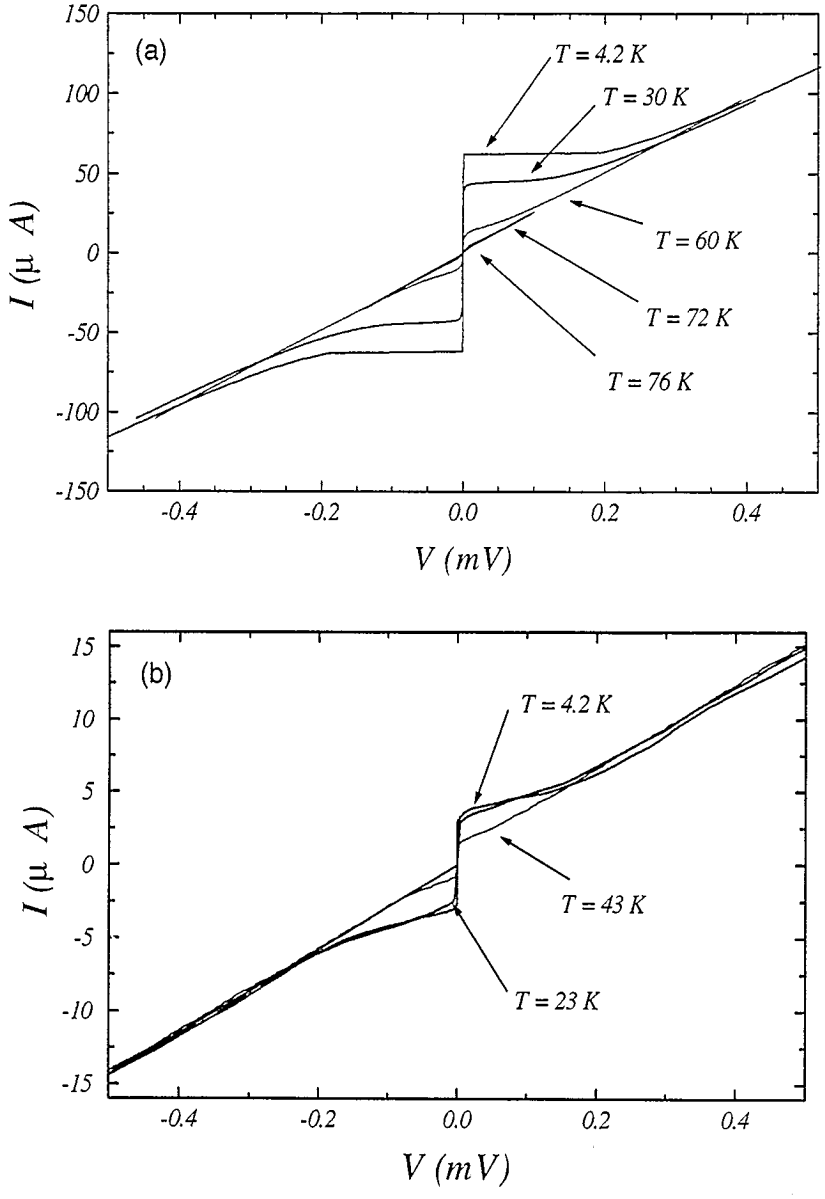

Fig. 7. *I–V* characteristic of a 16 μm large junction taken at different temperatures for a sample fabricated on a) $SrTiO_3$ and on b) sapphire, respectively.

Table 3
T_c and FWHM values of the (103) YBCO pole figures collected on the different stacking sequence

	$SrTiO_3$		Al_2O_3	
	Without MgO	With MgO	Without MgO	With MgO
T_c	91	86	85	82.5
$FWHM_\phi$	2.0°	2.5°	1.6°	1.4°
$FWHM_\chi$	4.0°	4.0°	6.8°	7.2°

A detailed analysis carried out on the whole multilayer structure gives, for the different layers, the epitaxial relationships reported in Table 2. As expected, on one part of the sample, the topmost CeO_2 and YBCO layers are 45° in-plane rotated with respect to the other part. This behavior leads to the formation of the artificial GB located at the interface between the unetched and the etched side of the sample. Table 3 reports the peak extensions (FWHM) in the pole figure together with the T_c values of the YBCO films deposited over the different stacking sequence. By comparing similar FWHM's for both sides of each sample, the $FWHM_\phi$ values show that the epitaxial relationships are respected in the order of 2°. On the other hand, looking at samples fabricated on different substrates, we note that the diffraction peaks obtained on ALO are wider than those obtained on STO, indicating a degree of structural perfection substantially lower for the YBCO deposited on the former substrate. Since the YBCO obtained on CeO_2 buffered sapphire generally exhibit excellent structural properties [11], the origin of disorder probably reside in the complex stacking sequence which involve several layers. It is worth noting that for YBCO on bare STO, FWHM's of 1.53° in χ and of 0.95° in ϕ are currently obtained [10]. In this latter case the $FWHM_\chi$ is nearly doubled compared to the former STO substrate sample. This is attributed to the twin formation in the rhombohedral structure of the ALO giving rise to the formation of faceting at the surface, which is propagated in the stack. This behavior is clearly visible, for example, on the surface of $LaAlO_3$. On such a substrate, $FWHM_\chi$ as great as 10° have been already observed even with no $FWHM_\phi$ more than 2° [10].

3.2. Electrical characterization

As reported in Table 3, all the films exhibit a T_c higher than 80 K but two different behaviors can be observed. First, the T_c of the samples deposited on STO substrates are always higher than those on ALO. Meanwhile, the YBCO film deposited on the side where the MgO is present has a T_c slightly lower than the T_c of the other side, independently of the substrate nature. The correlation with the degree of the structural perfection became evident by comparing the FWHM of each set of peaks. As shown in Table 3, the larger the peaks the lower the T_c. Furthermore, due to the lattice mismatch with the other materials considered here, the MgO layer, even if thin, is the source of further structural disorder in the overhanging layers.

In Fig. 7 (a,b) we report the I–V characteristics taken at different temperatures for a typical junction fabricated on STO and on sapphire substrates, respectively. Under the application of a microwave irradiation the junctions show several Shapiro steps. As already reported, by changing the radiation intensity, the critical current of the junction follows the Bessel behavior as a function of the power [6]. The obtained I–V characteristics of the junctions exhibit

Table 4
Electrical parameters of the Josephson junctions fabricated on $SrTiO_3$ and R-plane Al_2O_3 at different temperatures. For comparison, same preliminar results obtained on a junction fabricated on a 45° bi-crystal substrate are reported

Substrate	T (K)	J_C (A/cm^2)	$R_N A$ ($\Omega\cdot\mu$m^2)	$I_C R_N$ (μV)
$SrTiO_3$	4.2	3.1×10^3	9.1	282
bi-epitaxial	30	1.9×10^3	9.0	170
	60	3.8×10^2	8.2	31
	76	2.5	7.9	2
Al_2O_3	4.2	1.4×10^2	56	60
bi-epitaxial	23	9.4×10^1	58	54
	42	1.2×10^1	60	7.5
$SrTiO_3$	4.2	6.6×10^3	3.0	221
45° bicrystal	30	6.1×10^3	2.9	193
	60	1.1×10^3	2.5	31
	77	3.8×10^1	2.5	1.1

RSJ behavior independently of the substrate type. As reported in Table 4, the normalized resistance, taken on the device biased at 2 mV (i.e. far above $I_C R_N$), do not change significantly with the temperature. By comparing the values for our two samples with those measured on a series of junctions fabricated on a 45° tilted STO bi-crystal, we note that, for the bi-epitaxial GB junctions, the $R_N A$ values are always higher. With respect to the latter values, $R_N A$ about three times and one order of magnitude for the devices on STO and sapphire substrate, respectively. This behavior indicates either a more insulating barrier or a thicker barrier correlated with structural and/or morphological defects.

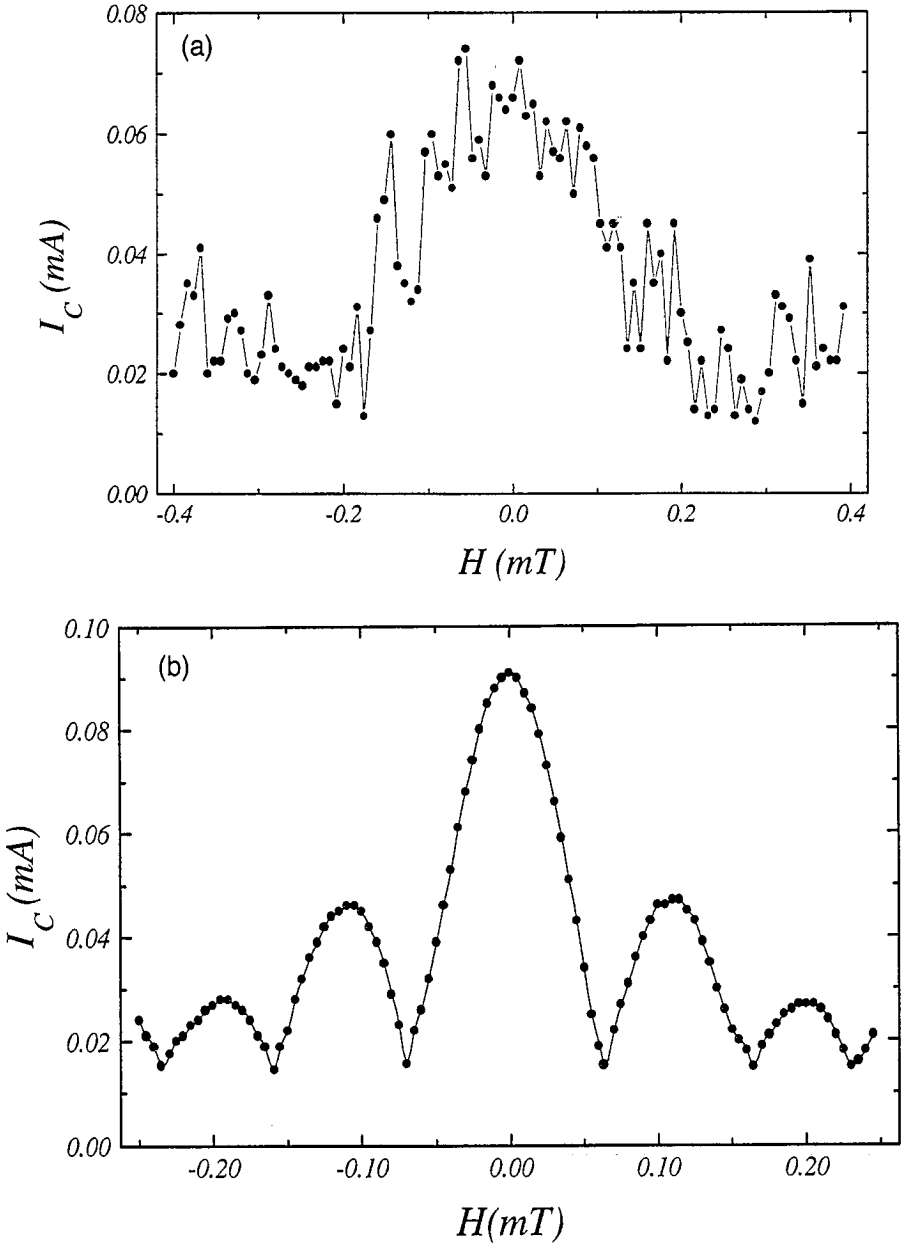

Fig. 8. I_C vs. H curve obtained on a) a 16 μm large junction fabricated on STO substrate and on b) a 5 μm large junction fabricated on 45° symmetric STO bi-crystal. The data were collected at 4.2 K.

To account for the weak link behavior of the GB two models are currently proposed: the model of the Insulating Barrier at the GB interface presented by Gross et al. [12] and the Two Channels model presented separately by Moeckley et al. [13] and by Sarnelli [14]. In these models, the weak link behavior of the GB is correlated to a defective layer at the interface between the two grains. Actually, the origin of this layer is generally ascribed to deviations from the bulk stoichiometry or to the structural disorder associated with the GB itself, but this occurrence is still unproven [15]. The reduction of J_C across the GB is therefore correlated with the spatial extent of this region or, in other words, with the effective thickness of the barrier in the Josephson junction. In this general frame, as much as the YBCO layer itself is defective as much as the interface is defective and as much as the order parameter will be reduced across the GB. Hence, we can explain the electrical behavior of our devices by considering the results of Table 3. The effective thickness of the barrier is correlated with the degree of structural perfection YBCO of the electrodes close to the GB. Consequently, as the structural perfection of the superconducting layer decreases the R_N of the junction increases.

In Fig. 8 we report a typical I_C vs. H curve obtained respectively on a 16 μm large junction fabricated on STO substrate and on a 5 μm large junction fabricated on 45° symmetric STO bi-crystal. The data were collected at 4.2 K. Since the Josephson penetration depth λ_J, as calculated from Table 4, is about 5.5 μm for the bi-epitaxial sample and about 3.8 μm for the bi-crystal sample, we expect, for these devices, the typical Fraunhofer-like I_C vs. H pattern for small uniform junctions ($w/\lambda_J \leq 4$) [16]. As it can be seen from these figures, for the bi-epitaxial I_C is modulated by the magnetic field, but the diffraction pattern largely deviates from the expected behavior. Meanwhile, the curve obtained on the bi-crystal junction shows the typical $\sin(x)/x$ pattern with symmetric periodic lobes.

As already discussed by Copetti et al. [17] and by Hilgenkamp et al. [18], the non-periodical dependence of I_C on the magnetic field and the strong reduction of J_C in GB-based devices can be well accounted for by considering the mutual occurrence of the $d_{X^2-Y^2}$ symmetry of the order parameter in HT_C materials and the microscopic faceting structure of the GB. Moreover, following the discussion carried out in these references, a similar behaviour is expected for symmetric GBs. On the contrary, our data show that a periodic pattern can be obtained even for high angle GBs.

On the other hand, Itzler and Tinkham recently discussed the role of random occurring defects inside the barrier on the electrical behavior of the junction under magnetic field [19]. They were able to demonstrate that the pinning of the Josephson vortices by the defects can interact with the electrical behavior of the device. The action is double: they reduce the carried current and they change the phase along the junction. Therefore, the I_C vs. H pattern is significantly modified by the presence of these pinned vortices in the barrier.

Since the electrical and magnetic performances of the devices increases as the structural perfection of YBCO layer increases, our results are in better agreement with this second model.

4. Conclusions

YBCO Josephson junctions, based on artificially generated in-plane bi-epitaxial grain boundaries, on $SrTiO_3$ and buffered R-plane sapphire were fabricated and characterized. The obtained devices followed the Resistively Shunted Junction model independently off the substrate type, showing Shapiro steps under microwave irradiation and critical current modulation under magnetic field. By comparing the obtained results with those obtained on a 45° bi-crystal, the Josephson current density of the junctions fabricated on sapphire substrates were largely depressed, while those of the devices on STO was only slightly below.

X-ray diffraction and High Resolution Electron Microscopy analyses showed that the structural and textural perfection of the YBCO film decreases as the complexity of the stacking sequence increases. The critical temperature is shown to be correlated to the orientation deviations.

Taking into account the structural properties of the YBCO film on the different stacking sequences, we can explain the behavior of our devices by treating the GB as a conventional Josephson struc-

ture where the barrier transparency is correlated with the degree of structural and textural perfection of each electrode, justifying the correlation between the normalized junction resistance $R_N A$ and the degree of disorder in the superconducting electrodes.

Acknowledgements

Stimulating discussions with R. Gross (University of Köln) are acknowledged. H.-R. Wenk (University of California, Berkeley), is greatly acknowledged for his critical review of the work. This work was partially supported by the ESPRIT Basic Research Project n. 7100. One of the authors (S.N.) undertook this work in the frame of the CEE-HCM program project n. ERB4001GT933579.

References

[1] K. Char, M.S. Colclough, S.M. Garrison, N. Newman and G. Zaharchuk, Appl. Phys. Lett. 59 (1991) 733.
[2] P. Chaudhari, J. Mannhart, D. Dimos, C.C. Touri, J. Chi, M.M. Oprysko and M. Scheuermann, Phys. Rev. Lett. 60 (1988) 1653.
[3] R. Gross, Proc. Int. Workshop on HTS Electron Devices, Whistler Mountain, Canada (1994), 19 and refs. therein reported.
[4] A. Beck, A. Stenzel, O. Froelich, R. Gerber, R. Gerdermann, L. Alff, B. Mayer, R. Gross, A. Marx, J.C. Villegier and H. Moriceau, IEEE Trans. Applied Superconductivity 5 (1995) 2192.
[5] F. Wang, G. Kunkel, C. Copetti, H. Kohlstedt and R. Wördenweber, Proc. EUCAS'93, ed. K. Sremyhrdt (DGM, Göttingen, 1993).
[6] S. Nicoletti, H. Moriceau, J.C. Villegier and D. Chateigner, Physica C 242 (1995) 99.
[7] J.C. Villegier, H. Moriceau, H. Boucher, R. Chicault, L. Di Cioccio, A. Jäger, M. Schwerdtfeger, M. Vabre and C. Villard, IEEE Trans. Magn. 27 (1991) 1552.
[8] L.G. Schulz, J. Appl. Phys. 20 (1949) 1030.
[9] M. Pernet, D. Chateigner and P. Germi, J. Alloys & Comp. 195 (1993) 149.
[10] D. Chateigner, Ph.D. Thesis, Université Joseph Fourier, 1994.
[11] L. Correra, S. Nicoletti, F. Arcidiacono and S. Neri, in ESPRIT BRA Project no. 6625 "X Band SRO" – Final Report.
[12] R. Gross and B. Mayer, Physica C 180 (1991) 235.
[13] B.H. Moeckley and R.A. Buhrman, IEEE Trans. on Appl. Sup. 5 (1995) 3414.
[14] E. Sarnelli, Interface Science 1 (1993) 287.
[15] See for example: A. Alarco, E. Olsson, Z.G. Ivanov, D. Winkler, E.A. Stepantsov, O.I. Lebedev, A.L. Vasiliev, A.Ya. Tzalenchuk and N.A. Kiselev, Physica C 247 (1995) 263.
[16] Physic and Applications of the Josephson Effect, A. Barone and G. Paternó (Wiley, New York, 1982).
[17] C.A. Copetti, F. Rüders, B. Oelze, Ch. Buchal, B. Kabius and J.W. Seo, Physica C 253 (1995) 63.
[18] H. Hilgenkamp, J. Mannhart and B. Mayer, Phys. Rev. B (to be published).
[19] M.A. Itzler and M. Tinkham, Phys. Rev. B 53 (1996) 11949.